Applied Thermal Engineering 171 (2020) 115126

Contents lists available at ScienceDirect

Applied Thermal Engineering

journal homepage: www.elsevier.com/locate/apthermeng

Thermal management of lithium-ion battery cells using 3D printed phase change composites

Malek Nofal[a], Said Al-Hallaj[b], Yayue Pan[a,*]

[a] University of Illinois at Chicago, Department of Mechanical and Industrial Engineering, 842 W Taylor Street, Chicago, IL 60607, United States
[b] AllCell Technologies, 2321 W 41st Street, Chicago IL, 60609, United States

HIGHLIGHTS

- Passive thermal management system of Lithium-ion cells.
- Expanded graphite/paraffin wax phase change composite fabrication.
- Selective laser sintering 3D printing technique without post-processing.
- Experimental and Finite Element Analysis validation of the fabricated composite.
- Customizable material composition based on the application.

ARTICLE INFO

Keywords:
Phase change materials
Thermal management
Lithium-ion battery
3D printing
Selective laser sintering
Paraffin wax/expanded graphite composite

ABSTRACT

This paper investigates the thermal management performance of a newly developed phase change composite for Lithium-ion battery packaging applications. Phase change materials have been investigated for passive thermal management of lithium-ion batteries on maintaining a uniform temperature, reducing the operational risk possibility, and elongating the life cycle. Despite these advances, the manufacturing of such material for battery thermal management is still not simple. Challenges including material waste, limited design freedom, and long production time remain and significantly limit the broader application of phase change materials in thermal management. To address those challenges, the phase change composite in this paper was produced using a 3D printing technique called selective self-binding laser sintering. The effectiveness of the 3D printed composites on thermal management of lithium-ion battery cells is investigated and compared with other phase change composites manufactured by conventional techniques. The composite studied in this paper consists of expanded graphite and paraffin wax. Equivalent heat generations of a cylindrical 18,650 Lithium-ion cell are resembled using a thin polyimide heater, and performances of the composites in thermal management are characterized. Experimental results and finite element analysis show that the 3D printed phase change composite can achieve thermal management functions comparable with the composites manufactured by the conventional press and soak technique.

1. Introduction

Due to the significant interest in powertrain electrification as an effort for United States energy independence, the energy density of Lithium-ion (Li-ion) batteries have been doubled in the last decades, allowing for more compact and efficient battery-powered goods, such as drones, portable electronics, and renewable energy storage [1,2]. During regular charging and discharging cycles, Li-ion batteries experience temperature elevation, which is found to be the primary cause of the performance degradation or capacity fade. For example, Waldmann et al. [3] showed that high temperatures accelerate the cathode electrode degradation and consequently lead to capacity fade in Li-ion batteries. Ramadass et al. [4] studied the effect of capacity fade under various ambient temperatures (25–55 °C), and they found that the capacity decreases down to 70% after 500 cycles at higher temperatures. Rao et al. [5] demonstrated that the life cycle of Li-ion battery could reach up to 3000 cycles at 45 °C, but at 60 °C the life cycle is only about 1000 cycles. In addition to the temperature rise, temperature non-uniformity within a cell and among cells in the battery pack can also cause adverse effects on the overall performance of the

* Corresponding author.
E-mail addresses: mnofal2@uic.edu (M. Nofal), salhallaj@allcelltech.com (S. Al-Hallaj), yayuepan@uic.edu (Y. Pan).

https://doi.org/10.1016/j.applthermaleng.2020.115126
Received 9 April 2019; Received in revised form 20 February 2020; Accepted 24 February 2020
Available online 25 February 2020

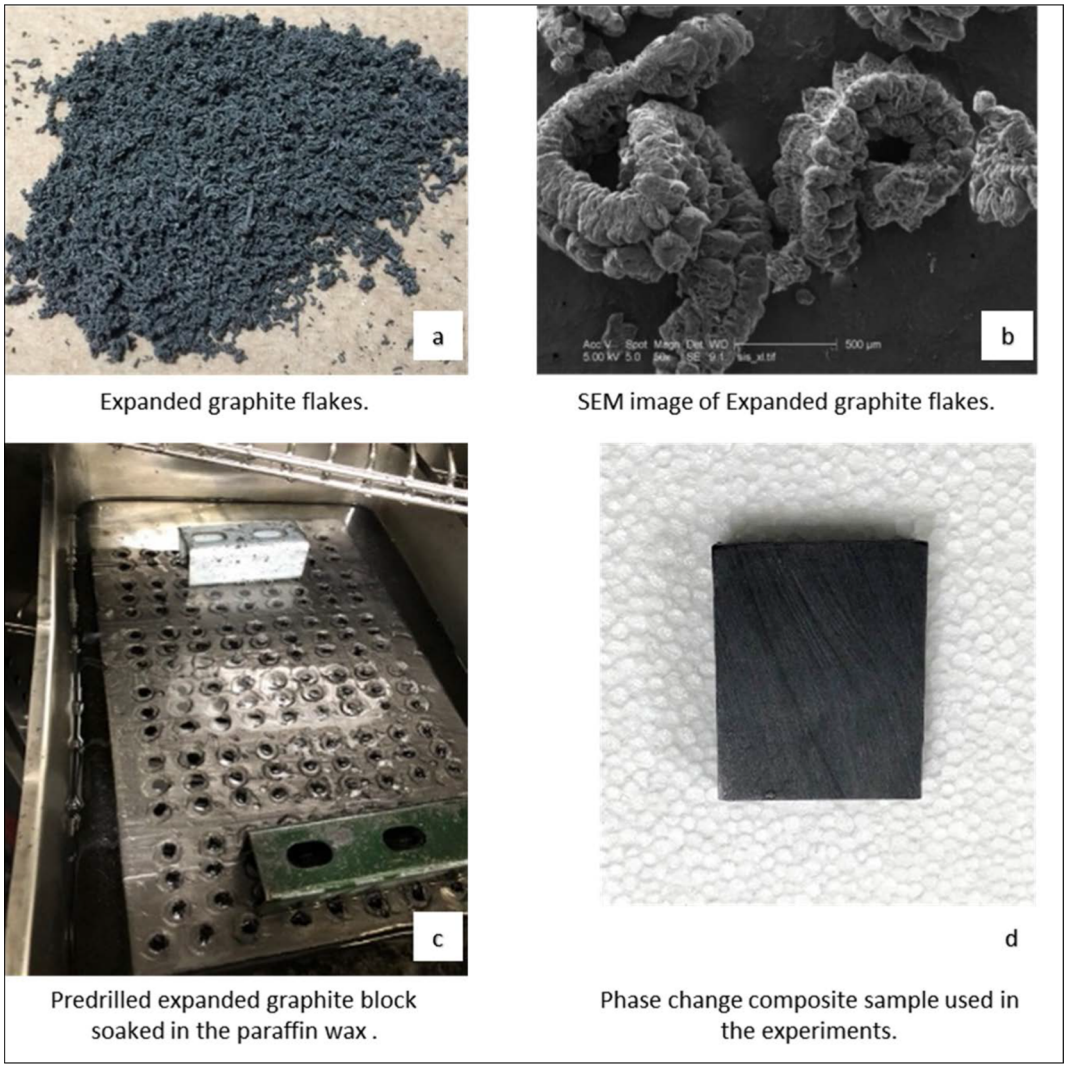

Fig. 1. Press-soak manufacturing process (a) a sample of the EG flakes. (b) an SEM image of the flakes that show the vermicular form [26]. (c) a predrilled expanded graphite block soaked in the paraffin wax bath at 75 °C. (d) a sample with dimensions of 27 × 20 × 1.7 mm ± 0.25 mm used in the experiments.

battery pack. Failures in the control of Li-ion battery cell temperatures can cause many problems, including performance degradation, capacity fade, fast charging risks, and severe thermal events such as explosions. Hence, the maximum temperature difference inside the battery pack usually has to be controlled within 5 °C, and high-temperature gradients among cells in a battery pack should be avoided [6].To achieve these temperature control objectives and ensure the optimal Li-ion battery operation performance, a thermal management system has to be used to dissipate the undesired heat quickly and uniformly, and to maintain battery cell temperatures within an allowable range. For feasible implementation and maintenance, the battery thermal management system should be lightweight, compact, and cost-effective. Also, it must present a low parasitic load and exhibit the ability to maintain the temperature uniformity of all cells in the battery pack [7].

Thermal management systems can be classified into two main categories. Active cooling, such as air and liquid cooling, that incorporates a mechanism of heat removal via forced air or circulating coolant in the Li-ion battery pack. Air cooling, for instance, is one of the simplest methods of heat dissipation due to its availability. On the other hand, liquid cooling can be achieved by either circulation of water-based coolant through cooling passages within the electronic device or flooding the device with a dielectric oil, which is then pumped out to a heat exchanger system. However, studies have shown that air as a heat transfer medium is not as effective as the liquid medium due to its lower thermal conductivity and limited heat capacity [8,9]. Although there are many advantages in the application of active cooling, these methods inherently make the overall system massive, complicated, and expensive to maintain. Also, there is a potential safety risk associated with liquid cooling systems as they must be sealed in order to prevent any form of leakage during operation [10,11].

The other category is passive cooling, such as heat pipes and phase change materials (PCM's) that rely, merely, on the thermo-dynamics of conduction to perform the heat transfer process. Recently, phase change materials and phase change composites (PCC's) have attained wide attention as perfect candidates for being integrated into the passive cooling systems of the battery pack [12–14]. When the battery pack is active (during the charging or discharging period), a portion of the dissipated heat is stored during the phase transition of the PCM (solid to liquid), and this heat is then released to the surrounding, during a period when the battery pack is resting. The stored heat during the process of phase change of PCM is called latent heat. The latent heat storage has many advantages, such as: (1) it is possible to store large amounts of heat with only small changes in temperature and, therefore, to have high storage density; (2) since the phase change occurs at a relatively constant temperature and it takes some time to complete, it becomes possible to smooth the temperature variations among battery cells. PCMs can store up to 14 times more heat per unit volume than sensible heat storage materials such as copper and aluminum [15]; (3)

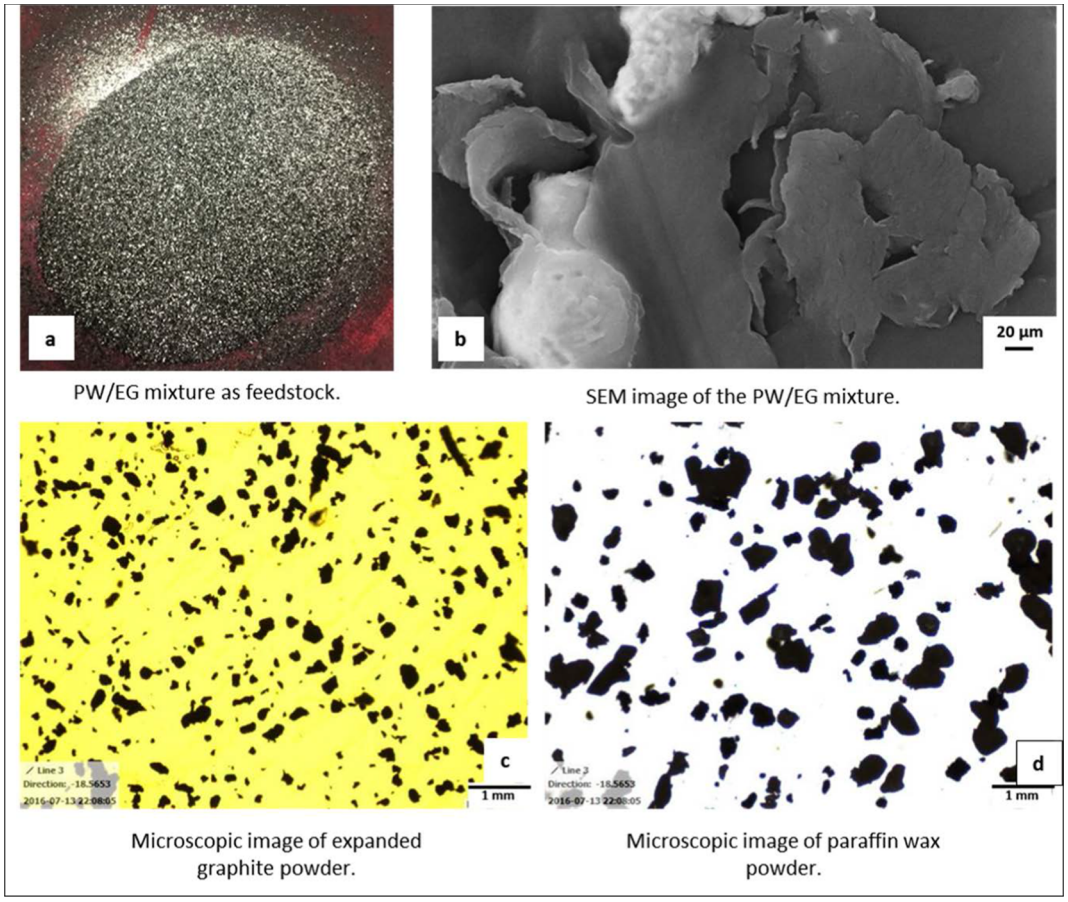

Fig. 2. Selective self-binding laser sintering process (a) Expanded graphite and paraffin wax mixture as a feedstock for the SSLS process. (b) SEM image of the mixture where the light particles are the paraffin wax powder and the dark particles are the expanded graphite powder. Microscopic images of (c) expanded graphite powder (d) paraffin wax powder with a particle size in the range of 50–200 µm.

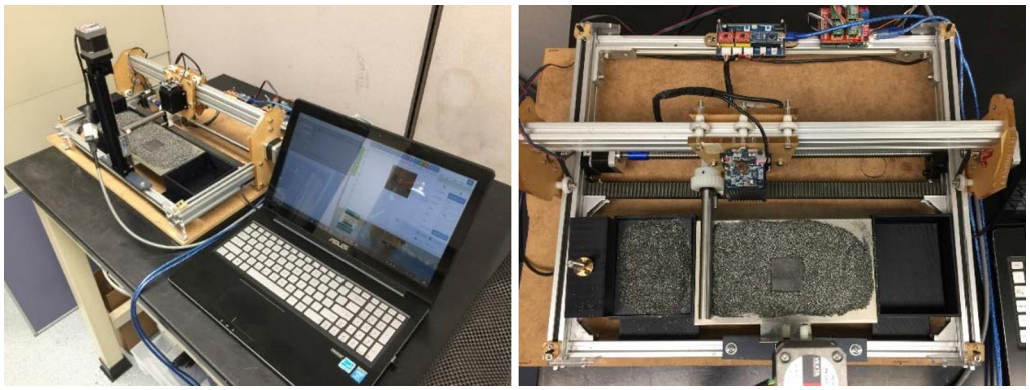

Fig. 3. Custom-made SLS machine with 5.5 W laser power, 0.25 mm scan spacing, and 50 $mm{\cdot}s^{-1}$ scan speed.

Another advantage of PCM is its low cost and availability [16]. However, most PCMs have poor thermal conductivities comparing to metallic materials. Therefore, highly conductive additives are filled into PCMs to form phase change material composites with enhanced thermal conductivities [17,18]. Among the many PCM composites for battery thermal management, paraffin wax/expanded graphite (PW/EG) composites have shown promising overall properties at a scaled-up level, especially, in Li-ion batteries applications [13,19]. In the PW/EG composite, paraffin wax (PW) – as the PCM material, is used for storing and releasing heat through its solid-liquid phase changes (latent heat) due to of its capability of solidifying and melting repeatedly without any phase segregation or latent heat degradation, relatively high latent heat capacity, a wide range of melting temperatures, low cost, and commercial availability. On the other hand, expanded graphite (EG) is used as the form-stable matrix because of its superior properties such as lightweight, high thermal conductivity, and its commercial availability.

Many manufacturing techniques for producing PW/EG composites have been reported in the literature. Sari et al. [20] studied the impregnation of paraffin into EG with different weight fractions of EG (2–10%). They found that 10% of EG, by weight, was suitable to construct a form-stable PW/EG composite. Also, increasing the weight fractions of EG from 2% to 10% has improved the thermal conductivity of the composite. Wu et al. [21] investigated the PW/EG composite for electronic thermal cooling applications. They stirred molten paraffin

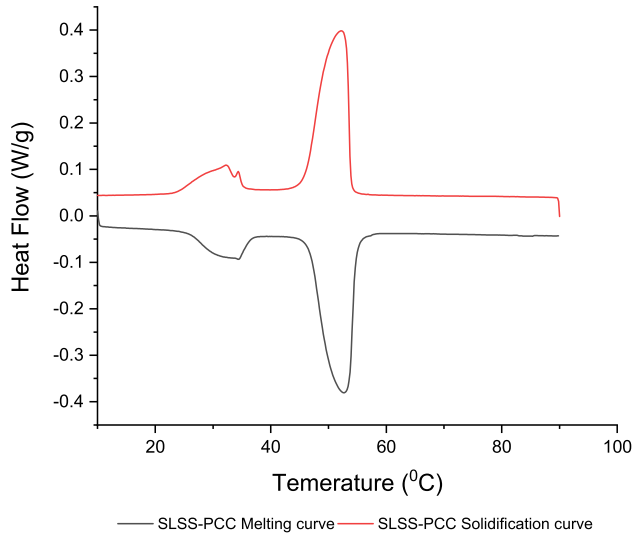

Fig. 4. Latent heat curves of SSLS-PCC in melting and solidification phases.

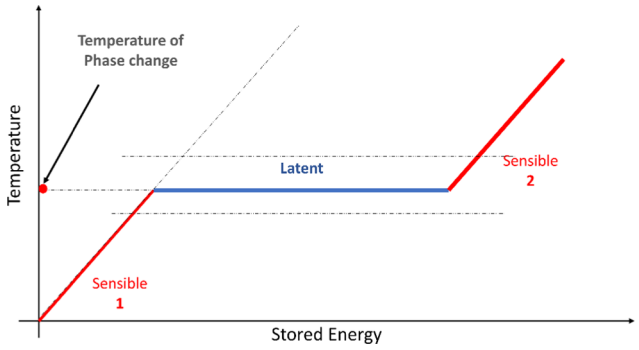

Fig. 5. Energy storage schematic of phase change composite.

Table 1
Summary of the average thermal properties for PS-PCC and SLS-PCC phase change composites.

Property	PS-PCC	SSLS-PCC
Thermal conductivity ($W{\cdot}m^{-1}{\cdot}K^{-1}$)	17.25 (In-plane)6.3 (Through-plane)	0.85
Specific heat capacity ($J{\cdot}g^{-1}{\cdot}K^{-1}$)	1.91	2.0
Latent heat capacity ($J{\cdot}g^{-1}$)	153	155
Density ρ ($kg{\cdot}m^{-3}$)	825	860

wax with 20% EG at a temperature above the wax melting point, which enabled them to enhance the thermal conductivity significantly (7.65 $W{\cdot}m^{-1}{\cdot}K^{-1}$ compared to 0·27 $W{\cdot}m^{-1}{\cdot}K^{-1}$ of the pure PW). Mills et al. [19] studied a manufacturing process in which EG was pressed into a matrix with different porosity levels and then soaked into a hot bath of PW to make the PW/EG composite. Using this manufacturing technique, they were able to fabricate a PCM composite with a thermal conductivity as high as 16.6 $W{\cdot}m^{-1}{\cdot}K^{-1}$. The PW/EG composite fabricated in Mills et al. work [15] was implemented in a passive thermal management system for Li-ion battery pack, and the results showed a significant improvement in the battery cycle life. Despite those advantages in manufacturing and applications of PW/EG composites, many limitations and challenges still remain, including: (1) the amount of time that takes to prepare the composite such as soaking time, mixture saturation, etc. is noticeably high; (2) machining processes such as drilling, milling, etc. are required to obtain the desired geometries, resulting in a lot of material waste; (3) custom cutting tools such as drill bits, endmills, and burrs are also required in order to match the cylindrical cell diameter ideally. Otherwise, air gaps will be present, and it will negatively affect the heat transfer mechanism between the cells and the composite [22].

To address these limitations, this paper investigates the thermal management performance of the PW/EG composite in lithium-ion battery packaging applications. The PCM composite was produced using selective self-binding laser sintering (SSLS) – a 3D printing technique, for the production of PW/EG composites. Additive manufacturing (AM), also known as 3D printing, offers multiple advantages over traditional manufacturing techniques, including almost near-zero material waste, rapid prototyping and reduced time to market, and construction of structures that are not possible with traditional manufacturing processes [23,24]. However, to the best knowledge of authors, there is no work about 3D printing of PW/EG composite reported in the literature by any other group yet. In our previous work, we successfully developed the SSLS 3D printing technique and fabricated PW/EG composite with various geometries [24]. The thermal, electrical, and mechanical properties of the PW/EG composite printed by our SSLS technique were characterized systematically, which suggest that the printed PW/EG composite is potentially promising for thermal management of Li-ion batteries.

Based on this previous work, the motivation of this paper is to investigate the effectiveness of 3D printed PW/EG composites for thermal management of Li-ion battery cells. In this work, to make a comparison, PW/EG samples were fabricated using both the SSLS 3D printing technique and the traditional press-soak manufacturing method [13]. Both composites have the same PW/EG ratio and dimensions. To investigate their performance, the equivalent heat generation of a cylindrical 18,650Li-ion cell is resembled using a polyimide heater. Different heat generation profiles were tested, and the corresponding thermal management results of the 3D printed PW/EG and traditionally fabricated PW/EG composites were recorded and compared. FEA simulation was performed and compared to the experimental results. The rest of this paper is organized as follows: The properties of phase change composites fabrication methods are presented in Sections 2.1 and 2.2. Heat generation calculations, experimental, and experimental setup are presented in Sections 2.3–2.5. Experimental and FEA results are presented in Section 3. Discussion and conclusion are given in Section 4.

2. Methodology

2.1. Phase change composite fabrication

A novel selective self-binding laser sintering (SSLS) technique has been successfully developed for 3D printing the PW/EG composite in our previous work [23,24]. To evaluate the effectiveness of the SSLS printed PW/EG composite in a thermal management system for Li-ion batteries, in this paper, we fabricated PW/EG composite samples using both the SSLS technique and the traditional press-soak technique [13]. In both manufacturing processes, paraffin wax from IGI (Titusville, PA) with a melting range (53.9–55.6 °C), and expanded graphite flakes from Superior Graphite (Chicago, IL) were used as feedstock for the production of PW/EG composite samples.

2.1.1. Press-soak (PS) manufacturing process

The press-soak process starts by producing the expanded graphite matrix by compacting the expanded graphite flakes using an automated press under a controlled pressure (50 psi, for 12 min). The graphite flakes are loaded manually into a hydraulic press (mass ~1.6 kg) to achieve a specific graphite block density (~180–250 $kg{\cdot}m^{-3}$). At that graphite block density, a balance of the maximum amount of PW impregnation, and a reasonable amount of soaking time can be achieved. For instance, any lower graphite densities would result in a very porous and fragile matrix with a risk of wax leakage. On the other hand, higher graphite block density would result in less PW impregnation and

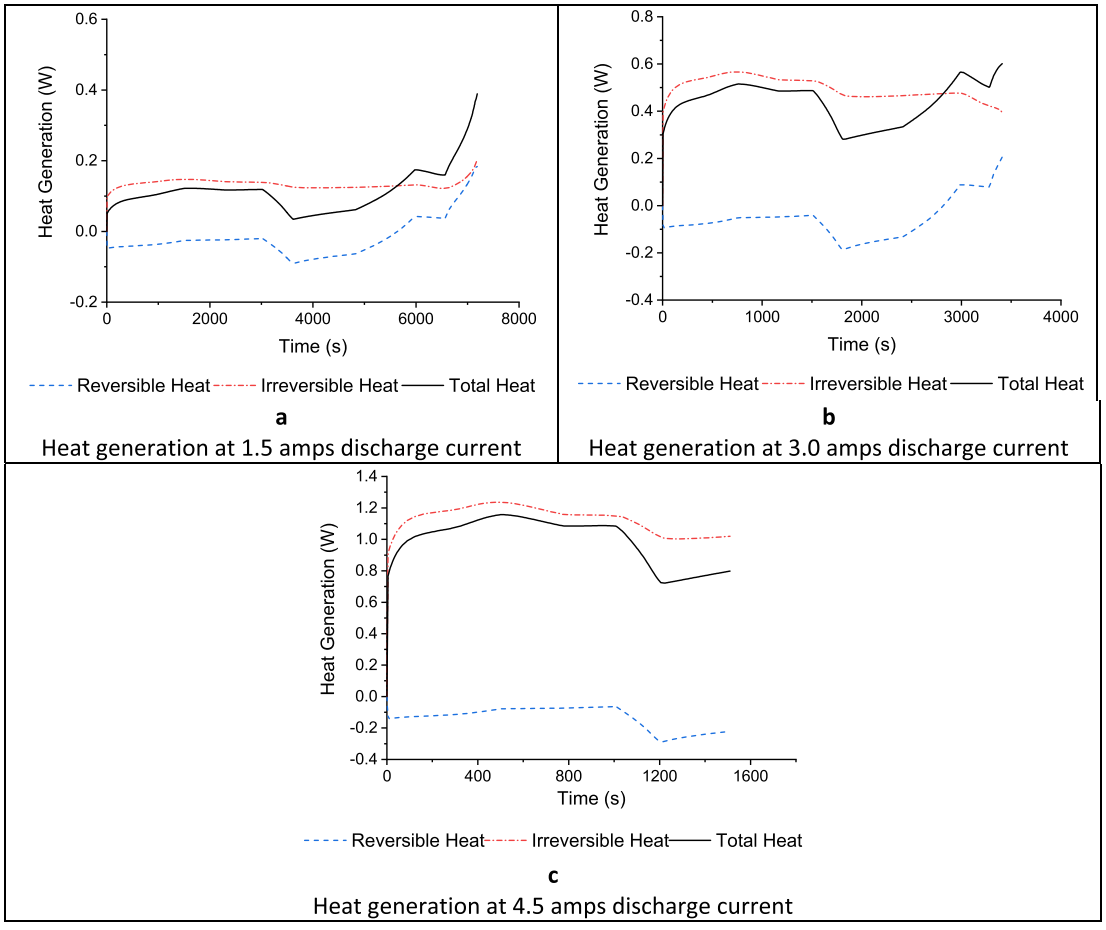

Fig. 6. Single Li-ion cell heat generation in Watts during discharging with different currents: (a) 1.5 amps. (b) 3 amps. (c) 4.5 amps.

Table 2
Equivalent heat generation for a single Li-ion cell at different discharge rates.

Current (A)	Average heat generation (W)	Equivalent voltage (V)	Time (s)
1.5	0.1	1.3	7200
3	0.5	2.9	3600
4.5	1	4.1	1800

significant soaking time due to the low porosity. Fig. 1(a) shows a sample of EG flakes, and (b) an SEM image of the flakes, which is in the vermicular form. After pressing the EG flakes into a block with the desired density, the EG block is then soaked into a hot bath of molten paraffin wax. The hot bath temperature is maintained in the range of 70–75 °C. During the soaking process, the molten wax impregnates into the graphite matrix through capillaries. Prior to this step, the graphite block is uniformly predrilled at various locations using a 12.7 mm drill bit to speed-up the impregnation process.

In this study, the soaking time was 48 h to maximize the PW ratio with a target of 75–80% by weight. This PW/EG weight ratio ensures an optimal balance of latent heat capacity, thermal conductivity, and form stability of the composite [25]. Fig. 1(c) shows the predrilled expanded graphite block soaked in the paraffin wax bath, and (d) shows the final phase change composite sample with dimensions of 27 × 20 × 1.7 mm ± 0.25 mm for the thermal management study in this paper.

2.1.2. Selective self-binding laser sintering (SSLS) process

In the selective self-binding laser sintering process, paraffin wax is selectively melted, and the molten PW acts as a binder to bind the expanded graphite particles together, and also is impregnated within the graphite particles at a micro level under the capillary forces.

To prepare feedstock for fabricating PW/EG composite using SSLS, EG flakes and PW were processed separately to make a fine powder of 50–200 μm particle size for the selective laser sintering process. A mixture of 80% PW and 20% EG by weight was tumbled for 2 h. Fig. 2(a) shows the final mixture composition, (b) shows an SEM image of the mixture, (c) and (d) show microscopic images of EG and PW powders respectively. The particle mixture is used as the feedstock in SSLS for the production of PW/EG composite.

A custom-made SSLS machine was used to fabricate the PW/EG composite, as shown in Fig. 3. It is equipped with a computer-controlled laser module (5.5 Watt) that scans the surface of the powder mixture selectively to form the composite using a back-and-forth scan pattern with a 0.25 mm scan spacing. The scan speed can be adjusted in the range of 1.5–50 $mm{\cdot}s^{-1}$ to tune the laser intensity for sintering PW with different melting degrees and, hence, different impregnation capabilities. With this setup and materials, it was determined that the optimal scan speed was 50 $mm{\cdot}s^{-1}$.

During the laser scanning, PW is melting because of the laser power in such a way that the capillary forces of the molten wax allow it to be impregnated within the EG particles and binds EG together when it solidifies.

2.2. Thermal properties of phase change composites

Phase change materials and composites are known for their thermal energy storage, specifically, latent energy storage. Moreover, Li-ion batteries operate in transient cycles with a low duty cycle, which means heat is produced during short periods of demanding use followed by more extended periods of idling or less active use. Therefore, phase

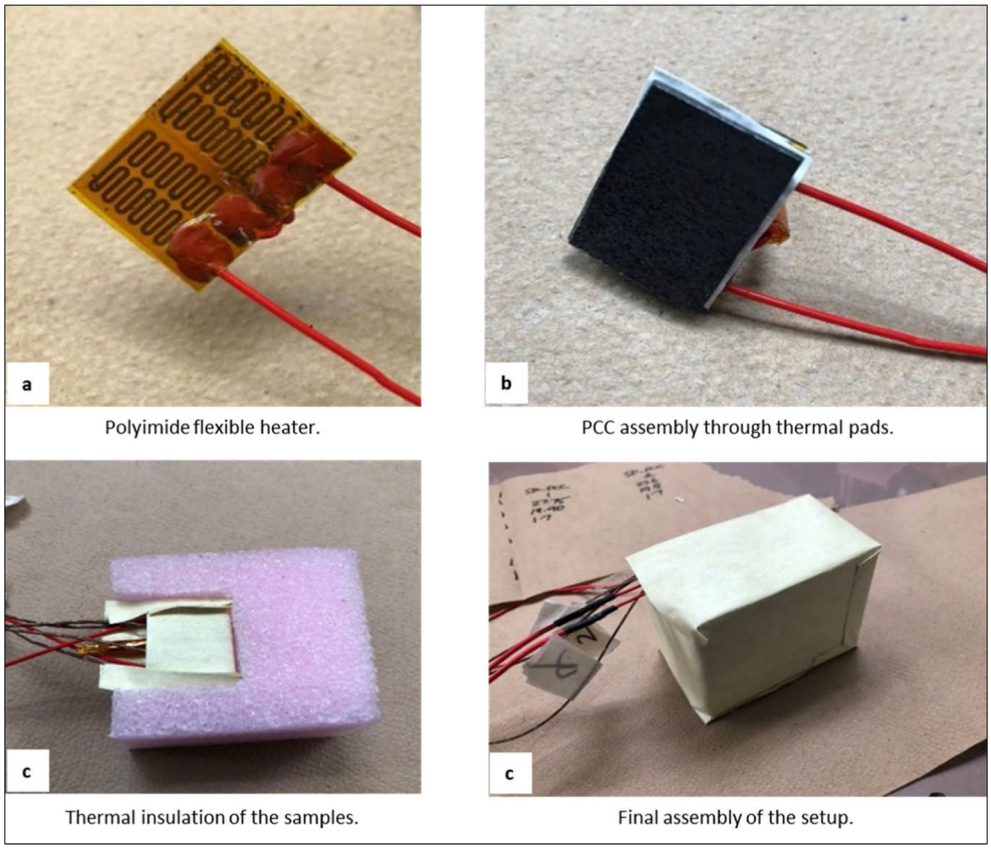

Fig. 7. Single cell heat generation setup. (a) Polyimide flexible heater. (b) Samples contact through thermal pads. (c) Thermal insulation of the samples. (d) Final assembly.

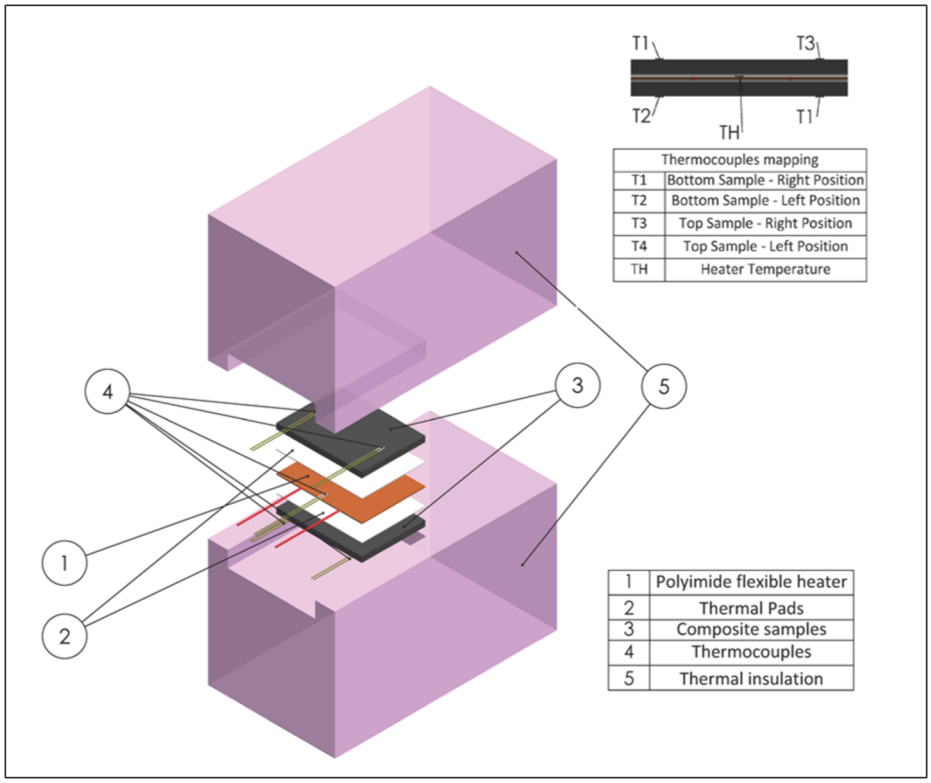

Fig. 8. Exploded CAD assembly of the setup.

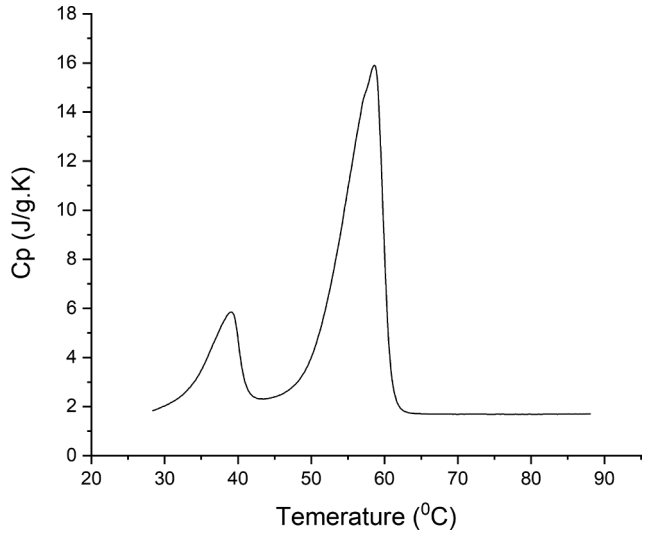

Fig. 9. Specific heat capacity of EG/PW phase change composite in $J{\cdot}g^{-1}K^{-1}$.

change composites are perfect candidates that can be integrated into the packings of Li-ion batteries as a passive thermal management system.

In the case of phase change material and composites, the thermal energy storage has two forms, sensible energy storage (SES) and latent energy storage (LES). Sensible energy is stored, naturally, by the mechanism of changing the object's temperature. The latent energy storage, the energy is stored during the phase change of the material. The amount of the stored latent heat is proportional to the change in enthalpy of fusion of the material and its mass. Fig. 4 shows the latent heat curves for the SSLS-PCC for melting and solidification phases at 1 $^{\circ}C{\cdot}min^{-1}$ ramp rate. Differential scanning calorimeter (DSC) apparatus (model DSC823e/700, manufactured by Mettler-Toledo) was used to measure the latent heat capacity. The mass of the specimen used in DSC was 10.2 mg, placed and sealed in a 40-microliter aluminum crucible.

As shown in Fig. 4, at 1 $^{\circ}C{\cdot}min^{-1}$ ramp rate, the average amount of latent heat is 1570 mJ, the latent heat capacity 155 $J{\cdot}g^{-1}$, the onset temperature 48 °C, and the peak temperature 53 °C. During the energy storage mechanism, the phase change composite utilizes some sensible energy above the PCM melting temperature [27] as shown in Fig. 5.

The total energy Q_{PCC} stored by the composite can be expressed as in Eq. (1):

$$Q_{PCC} = m_{PCC}\left[\int_{T1}^{Tm} C_{p,s}dT + H + \int_{Tm}^{T2} C_{p,l}dT\right] \quad (1)$$

where m_{PCC} is mass of the composite, $C_{p,s}$ and $C_{p,l}$ are specific heat capacities in solid and liquid phase respectively, H is the latent heat of fusion, T_1, T_m, and T_2 are the initial, melting, and final absolute temperatures. Table 1 shows the average thermal properties values for both composites tested in this study.

As shown in Table 1, both composites have similar thermal properties except for the thermal conductivity. Due to the self-binding principle of the SSLS process, when the paraffin wax particles melt during the laser scanning, it binds the expanded graphite particles, but it may also coat the graphite particles with a thin layer of wax, which may explain the lower thermal conductivity than the conventionally fabricated material PS-PCC [27].

2.3. Equivalent single cell heat generation

Li-ion cells are electrochemical devices where electrical energy is produced as a result of some chemical reactions occurring within the anode and cathode through the electrolyte. In these reactions, heat is generated as energy losses in the electrochemical energy conversion.

There are multiple approaches to estimating and modeling the heat generation of Li-ion cells. Electrochemical models [28–30] offer high accuracy in representing the battery internal electrochemical process; however, these models are complex and require in-depth knowledge of the battery chemical structure and properties [31]. Other models such as electric-equivalent circuit models [32–34] have proven a good level of accuracy on the Li-ion cell and the system level [35].

In this study, a model by Schweitzer et al. [14] was adopted based on a dimensionless assumption (0-D) or a lumped approach of the battery. The model assumes that the cells can be represented, solely, by its mass m_{cell} and specific heat capacity $C_{p,\ cell}$. Other factors such as convective heat coefficient h and surface area A are also considered in the case of convective heat loss. This assumption was justified due to the relatively low Biot number of small-form Li-ion cells, where conduction heat loss can be neglected [36].

The convective heat loss was ignored ($h \approx 0$) in the energy balance because the cell was assumed to be cycled in near adiabatic condition without any means of heat transfer to the phase change material nor the ambient. Thus, the energy balance equation yields the following:

$$(Q_{irr} + Q_{rev}) = m_{cell}C_{p,cell}\frac{dT}{dt} \quad (2)$$

Using Eq. (2), the heat generation of a single cylindrical 18,650 cell with a nominal capacity of 3.2 amp-hour was estimated during discharging with currents of 1.5 amps, 3.0 amps, and 4.5 amps, as shown in Fig. 6.

The total generated heat is the sum of the irreversible heat (Joule heating) and the reversible heat (entropic heating). It shows that the Joule heating is the primary source of cell heat generation comparing to the entropic one. In fact, the entropic heating absorbs some of Joule heating until a certain cell state of charge and then it adds to the total heating. Based on Fig. 6, the average heat generation in the 1.5 amps discharge was 0.1 W for 7200 s, 0.5 W for 3600 s in the case of 3.0 amps, and 1.0 W for 1800 s in the case of 4.5 amps.

The total thermal management heat balance can be expressed as shown in Eq. (3):

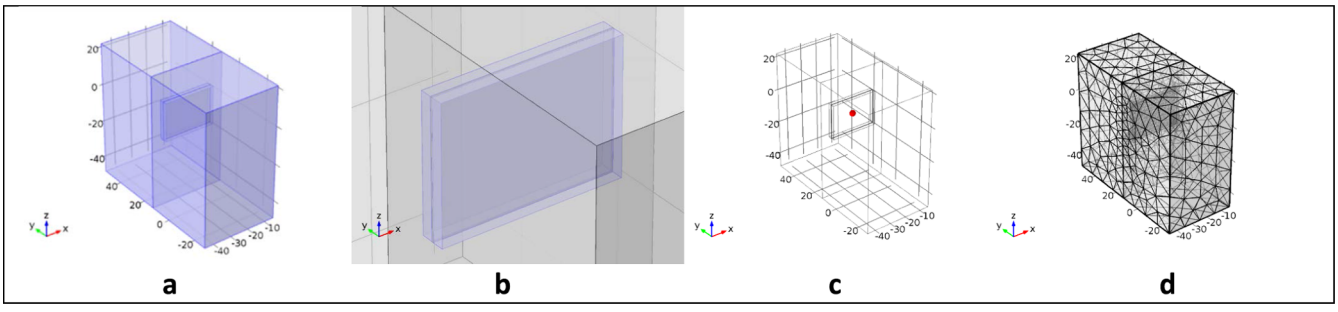

Fig. 10. FEA model setup. (a) Imported CAD geometry. (b) Composite domains definition. (c) Temperature probe locations. (d) Meshing the geometry.

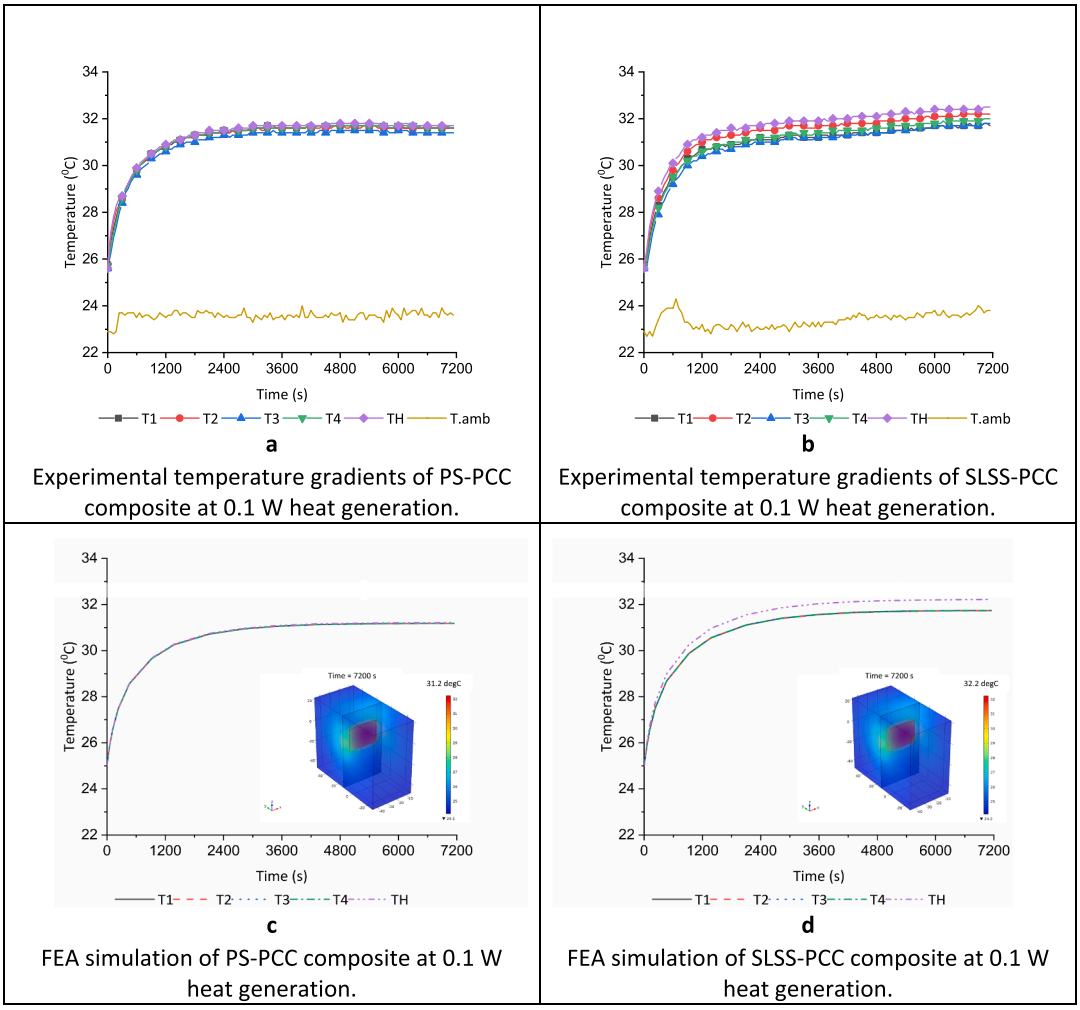

Fig. 11. Temperature gradients of phase change composite at 0.1 W heat generation for 7200 s. (a) Experimental PS-PCC. (b) Experimental SSLS-PCC. (c) FEA PS-PCC. (d) FEA SLSS-PCC.

$$\left[(I^2R_{int}) + \left(T_{cell}\frac{dV_{oc}}{dT}I\right)\right]\Delta t \triangleq m_{cell}\int_{T1}^{T2} C_{p,cell}dT + m_{PCC}\left[\int_{T1}^{Tm} C_{p,s}dT + H + \int_{Tm}^{T2} C_{p,l}dT\right] + \sum \dot{Q}_{loss} \quad (3)$$

In Eq. (3), the left-hand side denotes the resultant heat generation of the cell. Due to the small characteristic length of the cell which results in a small Biot number, the internal temperature gradient can be ignored, resulting in a thermally simple model [36,37]. The right-hand side denotes the amount of heat that the cell can absorb and the amount of energy that the PCC can store as sensible and latent heat as illustrated in Fig. 2. ΣQ_{loss} denotes all the heat losses to the insulation or the surrounding.

Based on the data from Fig. 6, a flexible polyimide electric heater was used (27 × 20 × 0.35 mm) with a fixed resistance (R = 17.2 Ω) at room temperature, to resemble the heat generation of a single cell. A DC power supply was used to control the amount of power the heater will dissipate into the composite. Three different heat generations were tested, denoted as low, medium, and high. In each case, the voltage was regulated based on Ohms law that can be expressed as $V = (PR)^{1/2}$; where V is the input voltage, P is the required power, and R is the heater resistance. Table 2 shows the voltage required for equivalent heat generations of a single cell.

2.4. Experimental setup

After preparing both composites (PS-PCC and SLSS-PCC) as discussed in Section 2.1, the electric heater was sandwiched between two identical composite samples. The samples had similar dimensions to the heater to ensure maximum heat transfer. Thermal pads were added on both sides of the heater (3M 8010) to maximize the surface contact with the composite samples. To ensure near-adiabatic conditions, the setup was insulated using insulation foam and thermal insulation wrap. K-type thermocouples were used to sense the temperature rise, and a portable data acquisition system (Yokogawa GP10) was used to monitor and record the temperatures. Figs. 7 and 8 show the experimental setup procedure.

2.5. FEA simulation setup

Finite element analysis was performed using the Heat Transfer Through Solid module in COMSOL Multiphysics v4.4. The CAD geometry in Fig. 8(e) was imported onto COMSOL in *.step* format. That yielded into five domains: 2x insulation materials (top and bottom), 1x heater, 2x PCC samples (top and bottom). Material properties such as thermal conductivity, density, specific heat capacity, etc. were defined for each domain. For the PCC, it is important to note that specific heat capacity C_p is a function of temperature. It can be estimated using the mass fraction method [23] or more accurately, it can be measured using a differential scanning calorimetry (DSC) apparatus. For the PW/EG

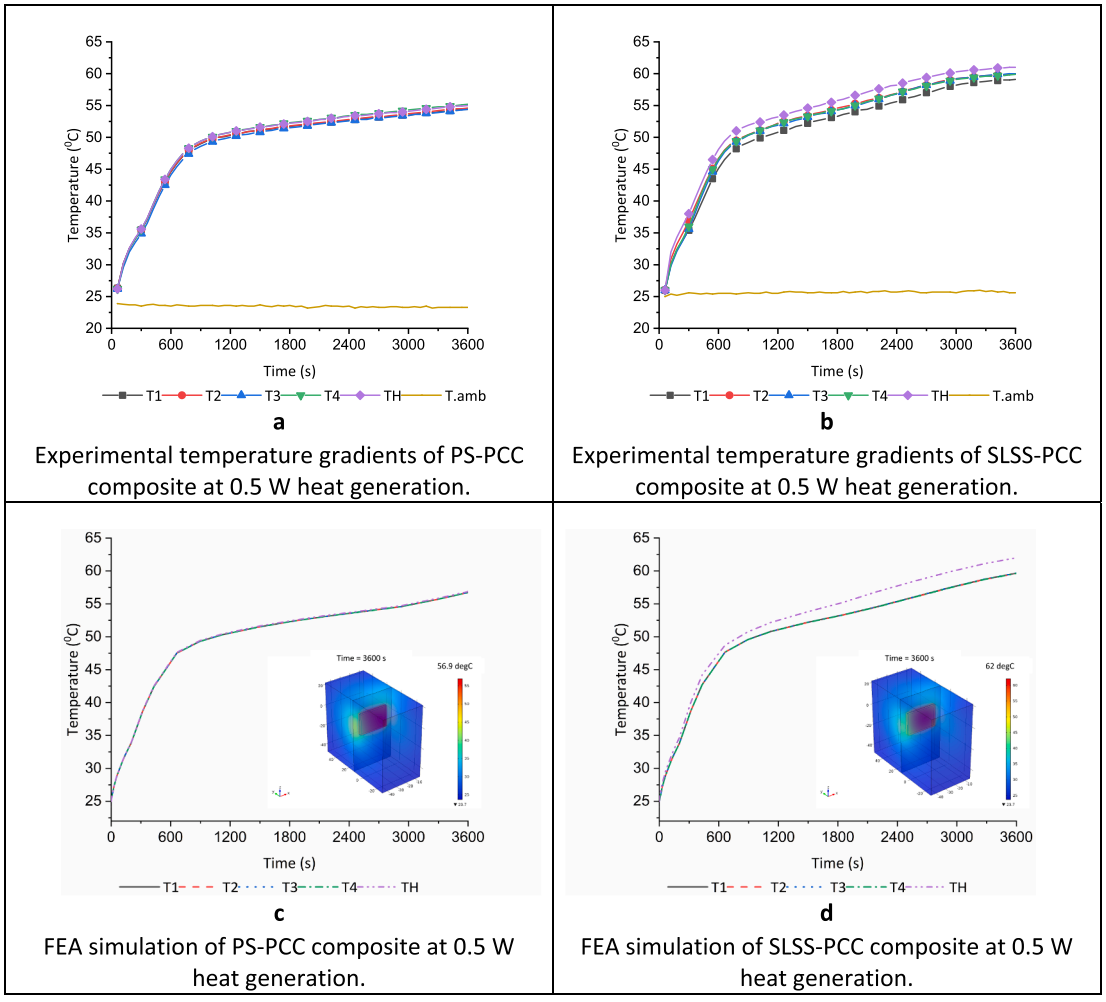

Fig. 12. Temperature gradients of phase change composite at 0.5 W heat generation for 3600 s. (a) Experimental PS-PCC. (b) Experimental SSLS-PCC. (c) FEA PS-PCC. (d) FEA SLSS-PCC.

composites used in this study, C_p was measured using DSC 204F1 Phoenix (manufactures by NETZSCH). Fig. 9 shows the measured C_p of the PW/EG phase change composite as a function of temperature. The thermal insulation wrap was defined as a virtual layer with its associated properties to simplify the computation. Also, a virtual air layer was defined between the heater and the top composite to represent the gap in the experimental setup. Temperature probes were located approximately on the sample spot as shown in Fig. 8(e). The heater was modeled as a heat source with a fixed power. Convective heat transfer or heat flux was also considered between the insulation and the ambient with a heat transfer coefficient of 10 $W{\cdot}m^{-1}\ K^{-1}$. Finally, the mesh was automatically generated with a normal mesh size. The overall model yielded into 10,496 tetrahedral elements and 2386 triangular elements. Fig. 10 shows the steps of the FEA setup.

3. Results

3.1. Low discharge rate (1.5 amps, 0.1 W)

In the case of low discharge current (1.5 amps), it is approximately 0.5x discharge rate of a single Li-ion cell. The heat generation is about 0.1 W for 7200 s. To match that heat generation, the voltage was set to ~1.3 V, as listed in Table 2. Fig. 11 (a) and (c) show the experimental and FEA temperature gradient results of PS-PCC. Fig. 11(b) and (d) show the experimental and FEA temperature gradient results of SSLS-PCC.

As shown in Fig. 11, at a low heat generation, both PS-PCC and SSLS-PCC demonstrate a similar heating profile. The slope for the sensible region is approximately identical. In the case of SSLS-PCC, the heater temperature is always the highest throughout the experiment. The temperature variation is very minimal (within 1 °C), but it is more significant than the variation in PS-PCC. In Fig. 11 (b), the bump in the ambient temperature (t: 300–900 s) did not affect the sensible region, which suggests proper insulation against any convection heat transfer. However, there might be a conduction heat transfer to the insulation foam, which must be investigated. The FEA results show similar curve profiles to the experimental ones in both PS-PCC and SLSS-PCC. The high heater temperature *TH* in the case of SLSS-PCC in Fig. 11(d) can be explained by the lower thermal conductivity of the composite.

3.2. Medium discharge rate (3.0 amps, 0.5 W)

In the case of the 3.0 amps cell discharge current, which is approximately 1x discharge rate of a single Li-ion cell, the heat generation is about 0.5 W for 3600 s. To match that heat generation, the voltage was set to ~2.9 V as listed in Table 2. Fig. 12(a) and (c) show the experimental and FEA temperature gradient results of PS-PCC. Fig. 12(b) and (d) show the experimental and FEA temperature gradient results of SSLS-PCC.

For the medium heat generation, both composites entered the latent region after 600 s and fully completed the phase change of PCM. A similar observation was noted where the variation is slightly more

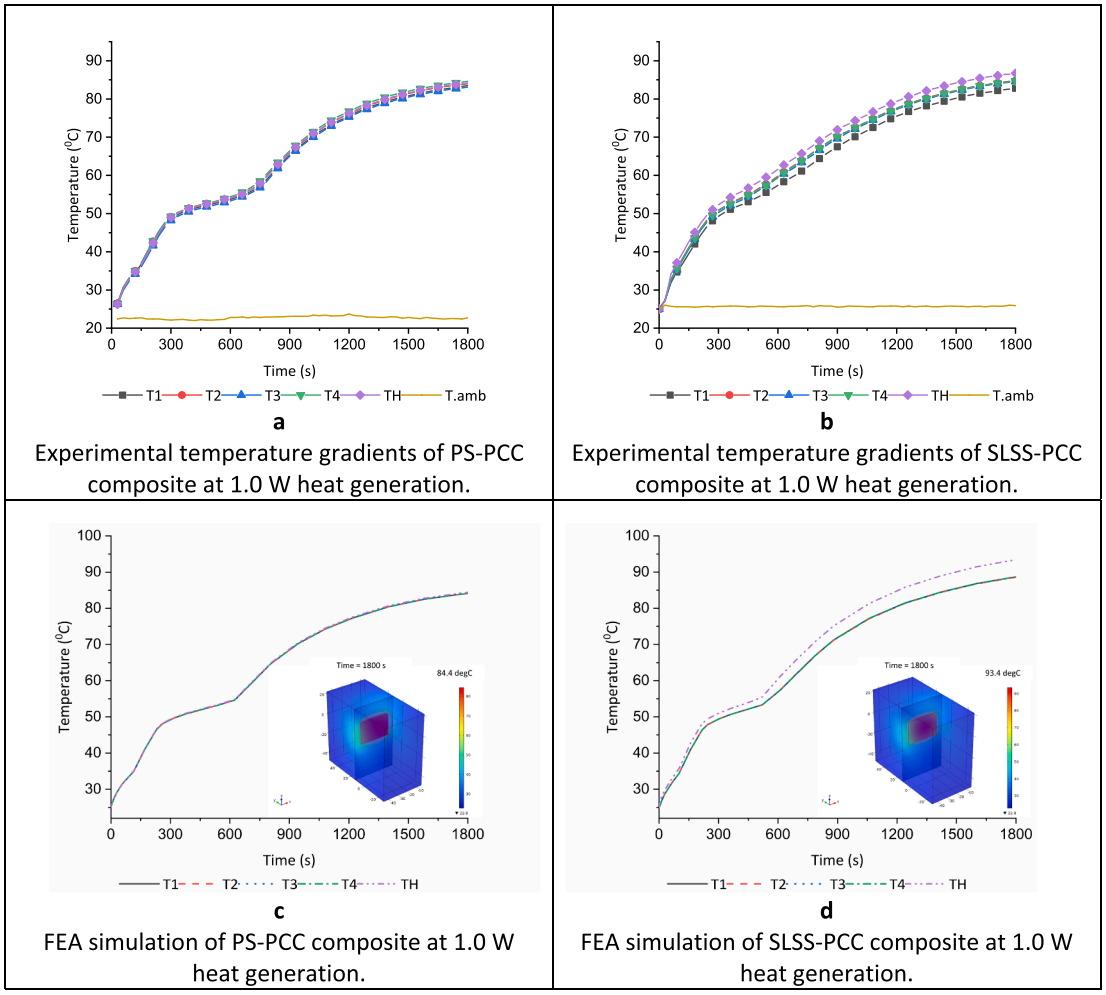

Fig. 13. Temperature gradients of phase change composite at 1.0 W heat generation for 1800 s. (a) Experimental PS-PCC. (b) Experimental SSLS-PCC. (c) FEA PS-PCC. (d) FEA SLSS-PCC.

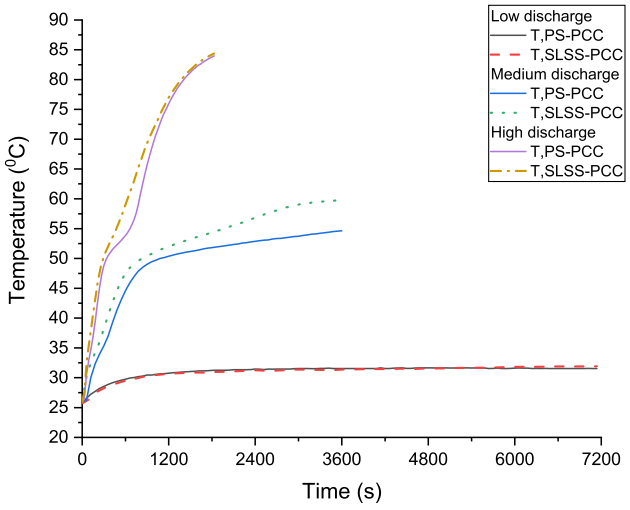

Fig. 14. Comparison of experimental results of PS-PCC and SLSS-PCC.

evident in the case of SSLS-PCC. It is mainly due to the slightly lower thermal conductivity of the SSLS-PCC in comparison with the PS-PCC. In Fig. 12(b), it shows that T1 (Bottom sample – Right position) is lower than the rest of the positions. This may be due to the close interface with the bottom thermal insulation foam that acts as a heatsink. However, it is not significant (less than 2 °C). Similarly, the FEA curves are in agreement with the experimental curves where TH is higher than the PCC temperature for the SLSS-PCC.

3.3. High discharge rate (4.5 amps, 1.0 W)

Finally, for the 4.5 amps cell discharge current, which is approximately 1.5x discharge rate for a single cell, the heat generation is about 1.0 W for 1800 s. To match that heat generation, the voltage was set to ~4.1 V as seen in Table 2. Fig. 13(a) and (c) show the experimental and FEA temperature gradient results of PS-PCC. Fig. 13(b) and (d) show the experimental and FEA temperature gradient results of SSLS-PCC.

In the high discharge rate, both composites have exceeded the latent region and entered the second sensible region. In Fig. 13(a), PS-PCC samples started phase change after 300 s and entered into the second sensible region after 600 s. Theoretically, the temperature must keep rising, but there was a heat loss to the surrounding through conduction to the insulation foam and convection to the ambient, and it can be seen after t = 1000 s. In Fig. 12(b), the same observations from the previous heat generation cases were noted. The higher variation confirms the effect of the lower thermal conductivity. Also, the mixture distribution and uniformity of the expanded graphite and paraffin wax may cause localized wax spots that have even lower thermal conductivities. Fig. 14 shows the comparison of the experimental results of PS-PCC and SLSS-PCC for each heat generation scenario (low, medium, and high).

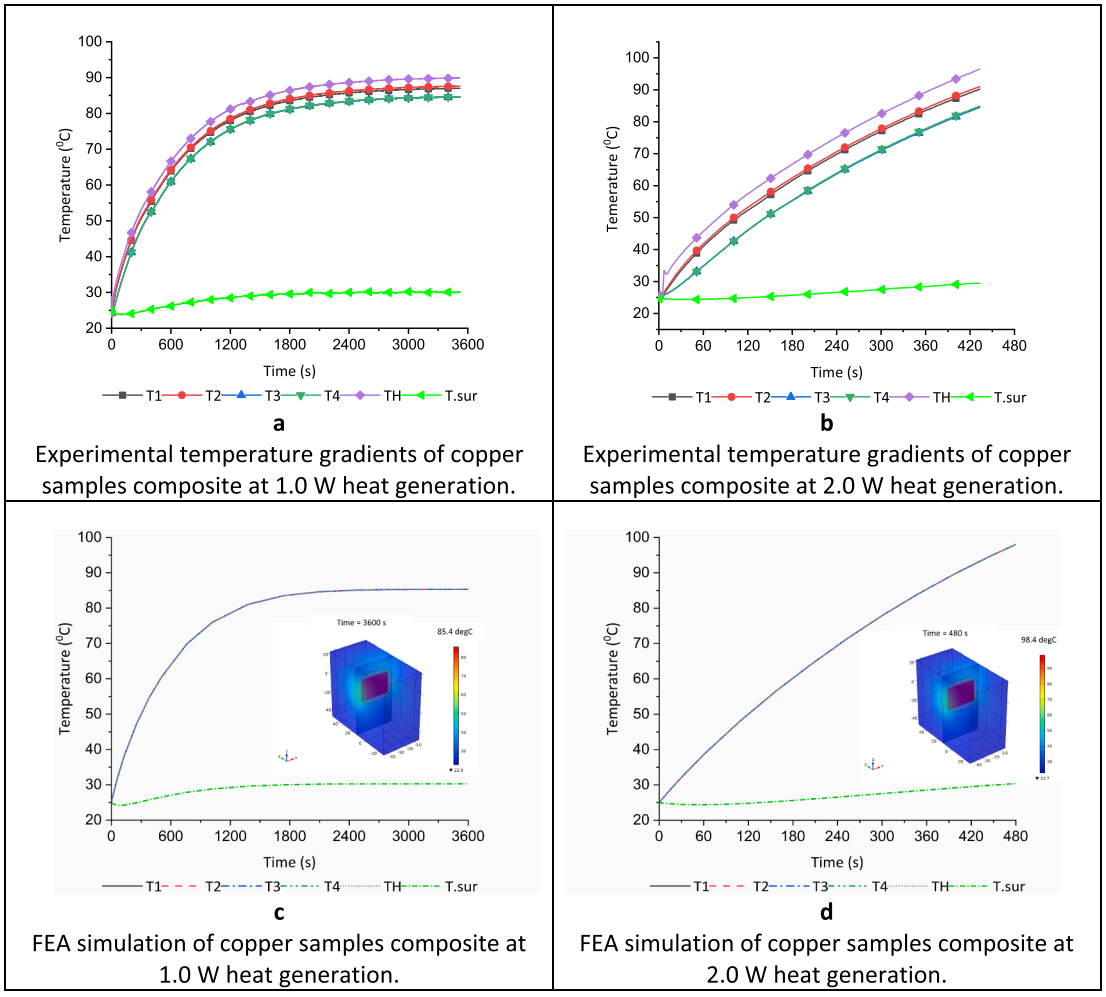

Fig. 15. Temperature gradient of copper samples (a) 1 W heat generation (b) 2 W heat generation.

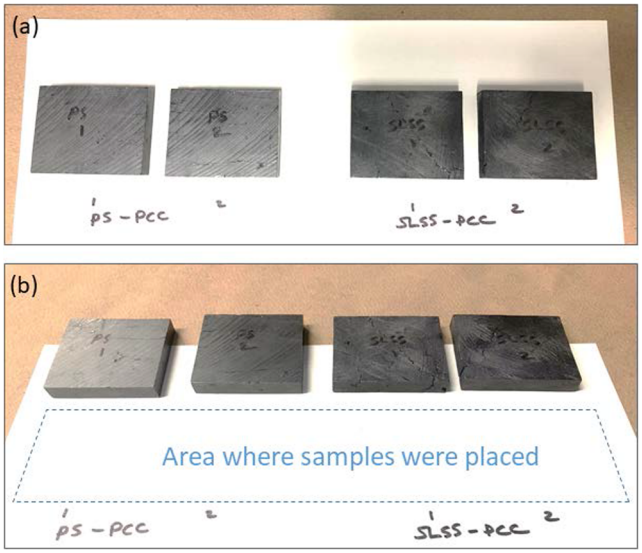

Fig. 16. Photos of PS-PCC and SLSS-PCC composite samples (a) before and (b) after cycling.

3.4. Heat loss to the ambient

To investigate the heat loss to the surrounding, other experiments and FEA simulations have been conducted using a copper sample that has the same dimensions as the phase change composite. 1 W, and 2 W heat generation cases were conducted with the same experimental setup. To observe the convection heat transfer effect, a thermocouple was placed on the outer surface of the setup as seen in Fig. 8 (d). The test duration was not constrained because the interest was to reach the steady-state to determine the heat loss. As in Li-ion cells, the test was terminated when the temperature reached ~90 °C because the cell will experience uncontrollable chemical reaction at this point.

From Fig. 15, it can be observed that there is heat loss to the environment explained by the steady-state temperature curves in Fig. 15(a). This means that the heat generated from the heater is completely dissipated away from the copper samples, mainly, to the insulation foam through conduction. Convection heat transfer from the ambient was also observed through the surface temperature rise (T. sur). The FEA simulation showed a narrower temperature variation across the copper samples and the heater. However, the curve profiles are similar in both cases.

3.5. Thermal stability performance

To investigate the thermal/form stability of the proposed phase change composite, PS-PCC and SLSS-PCC samples were cycled from 25 °C to 70 °C (~15 °C above the melting temperature of the paraffin wax of 55 °C) in a thermal chamber (model MicroClimate MCB-1.2 manufactured by Cincinnati Sub-Zero). The cycling steps were as follows:

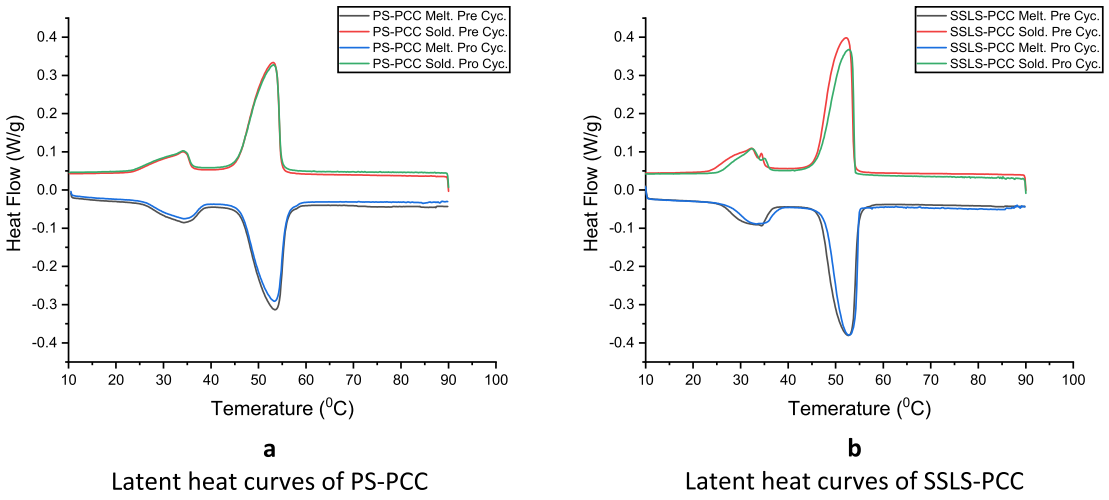

Fig. 17. Latent heat curves of (a) PS-PCC and (b) SSLS-PCC in melting and solidification phases before and after thermal cycling.

Step 1. Temperature Ramp: 25 °C to 70 °C within 600 s
Step 2. Hold Temperature at 70 °C for 1200 s
Step 3. Temperature Ramp: 70 °C to 25 °C within 600 s
Step 4. Hold Temperature at 25 °C for 1200 s
Step 5. Jump to Step 1. Repeat 20 times
Step 6. End.

Mass and dimension were taken before the cycling, after cycle 1, cycle 20. As shown in Fig. 16, no crack, leakage, or appearance change was observed in all samples after 20 heat-storing/releasing cycles, indicating both the PS-PCC and the SLSS-PCC are form stable.

Besides, the mass measurement results show a 0.04% mass loss for the PS-PCC and 0.05% for the SLSS-PCC after the first cycle, and a 0.04% mass loss for the PS-PCC and 0.14% for the SLSS-PCC after 20 cycles. This slight mass loss increase of SLSS-PCC after 20 cycles is mainly due to the nature of the SLSS process, in which the molten paraffin wax coats the external surface of the composite during the sintering. Compared to the recently reported PCC materials [38–43], such a mass loss is negligible and the SLSS-PCC significantly outperforms them, showing an excellent thermal stability which is comparable with the PS-PCC. Differential scanning calorimetry measurements were taken for the thermally cycled samples and compared the measurements before cycling as shown in Fig. 17.

In Fig. 17, the latent heat curves for both PS-PCC and SSLS-PCC showed similar behavior in both melting and solidification cycles in terms of latent heat capacity, onset and peak temperatures. The variation in melting curves in Fig. 17(a) and solidification curves in Fig. 17(b) are insignificant and can be explained by the method of manufacturing each composite.

4. Conclusions

In this paper, a PW/EG composite is 3D printed in a layer by layer manner by using selective self-binding laser sintering (SSLS) technique. The PW/EG composite consists of paraffin wax (PW) that has high latent heat capacity, and thermally conductive expanded graphite (EG). It is investigated for being integrated with Li-ion cells to achieve a passive thermal management system. Equivalent heat generations of a cylindrical 18,650 lithium-ion cell were resembled using a thin polyimide heater. Low (0.1 W), medium (0.5 W) and high (1 W) heat generations were tested using traditionally manufactured phase change composite (PS-SLS), and the SSLS printed phase change composite (SSLS-PCC) as a thermal management system. The PW/EG composite samples printed by using our new SSLS technique showed similar behavior with the traditionally fabricated PW/EG composite, regarding temperature rise in the composites. A slightly larger temperature variation is observed in the SSLS-PCC, which can be explained by its lower thermal conductivity in comparison with PS-PCC (0.85 and 17.2 W/m.K respectively). Also, the mixture distribution and uniformity of the expanded graphite and paraffin wax powder for selective laser sintering process may cause localized wax spots that have even lower thermal conductivities. Future work will optimize the manufacturing process to improve the SSLS-PCC thermal conductivity and address this limitation.

The experimental and finite element analysis results show that the PW/EG phase change composite fabricated by SSLS process (denoted as SSLS-PCC) can achieve thermal management functions comparable with the composites manufactured by the conventional press and soak technique as shown in Fig. 13. The SSLS-PCC offers excellent thermal properties that are very suitable as a passive thermal management system for Li-ion battery packs. Also, the self-binding selective laser sintering (SSLS) process offers many advantages over conventional processes in terms of manufacturing time, material waste, geometrical freedom, and more importantly, composite ratio (paraffin wax to expanded graphite ratio). These advantages enable the freedom of customizing the thermal, electrical, and mechanical properties of the PW/EG composites. Future work will include investigation of the SSLS-PCC for thermal management of full Li-ion battery packs with actual electrical cycles (charging and discharging) under various ambient conditions. Also, other applications will be investigated such as thermal energy storage systems and heat exchangers for onboard electric mobility and non-idling heating and cooling.

Declaration of Competing Interest

The authors declare that they have no known competing financial interests or personal relationships that could have appeared to influence the work reported in this paper.

Acknowledgement

The authors sincerely thank AllCell Technologies LLC. Chicago IL, for their support of this study.

Appendix A. Supplementary material

Supplementary data to this article can be found online at https://doi.org/10.1016/j.applthermaleng.2020.115126.

References

[1] D. Howell, S. Boyd, B. Cunningham, S. Gillard, L. Slezak, Enabling Fast Charging: A Technology Gap Assessment, 2017.
[2] N. Decker, North America Energy Independence, Ubs, 2018.
[3] T. Waldmann, M. Wilka, M. Kasper, M. Fleischhammer, M. Wohlfahrt-Mehrens, Temperature dependent ageing mechanisms in lithium-ion batteries – a post-mortem study, J. Power Sources 262 (2014) 129–135.
[4] P. Ramadass, B. Haran, R. White, B.N. Popov, Capacity fade of Sony 18650 cells cycled at elevated temperatures: Part II. Capacity fade analysis, J. Power Sources 112 (2) (2002) 614–620.
[5] Z. Rao, S. Wang, M. Wu, Z. Lin, F. Li, Experimental investigation on thermal management of electric vehicle battery with heat pipe, Energy Convers. Manag. 65 (2013) 92–97.
[6] C. Park, A.K. Jaura, Dynamic thermal model of Li-Ion battery for predictive behavior in hybrid and fuel cell vehicles, SAE Tech. Pap. (2003).
[7] A. Pesaran, Battery thermal management in EVs and HEVs : issues and solutions, Adv. Automot. Batter. Conf (2001) 10.
[8] P. Nelson, D. Dees, K. Amine, G. Henriksen, Modeling thermal management of lithium-ion PNGV batteries, J. Power Sources 110 (2) (2002) 349–356.
[9] S.C. Chen, C.C. Wan, Y.Y. Wang, Thermal analysis of lithium-ion batteries, J. Power Sources 140 (1) (2005) 111–124.
[10] G. Karimi, X. Li, Thermal management of lithium-ion batteries for electric vehicles, Int. J. Energy Res. 37 (1) (2013) 13–24.
[11] A.A. Pesaran, Battery thermal models for hybrid vehicle simulations, J. Power Sources 110 (2) (2002) 377–382.
[12] R. Sabbah, R. Kizilel, J.R. Selman, S. Al-Hallaj, Active (air-cooled) vs. passive (phase change material) thermal management of high power lithium-ion packs: limitation of temperature rise and uniformity of temperature distribution, J. Power Sources 182 (2) (2008) 630–638.
[13] S.A. Khateeb, M.M. Farid, J.R. Selman, S. Al-Hallaj, Design and simulation of a lithium-ion battery with a phase change material thermal management system for an electric scooter, J. Power Sources 128 (2) (2004) 292–307.
[14] B. Schweitzer, S. Wilke, S. Khateeb, S. Al-Hallaj, Experimental validation of a 0-D numerical model for phase change thermal management systems in lithium-ion batteries, J. Power Sources 287 (2015) 211–219.
[15] S. Raoux, W. Wełnic, D. Lelmini, Phase change materials and their application to nonvolatile memories, Chem. Rev. 110 (1) (2010) 240–267.
[16] A.H. Abedin, A critical review of thermochemical energy storage systems, Open Renew. Energy J. 4 (1) (2011) 42–46.
[17] A. Sari, Form-stable paraffin/high density polyethylene composites as solid-liquid phase change material for thermal energy storage: preparation and thermal properties, Energy Convers. Manag. 45 (13–14) (2004) 2033–2042.
[18] X. Fang, et al., Thermal energy storage performance of paraffin-based composite phase change materials filled with hexagonal boron nitride nanosheets, Energy Convers. Manag. 80 (2014) 103–109.
[19] A. Mills, M. Farid, J.R. Selman, S. Al-Hallaj, Thermal conductivity enhancement of phase change materials using a graphite matrix, Appl. Therm. Eng. 26 (14–15) (2006) 1652–1661.
[20] A. Sari, A. Karaipekli, Thermal conductivity and latent heat thermal energy storage characteristics of paraffin/expanded graphite composite as phase change material, Appl. Therm. Eng. 27 (8–9) (2007) 1271–1277.
[21] W. Wu, G. Zhang, X. Ke, X. Yang, Z. Wang, C. Liu, Preparation and thermal conductivity enhancement of composite phase change materials for electronic thermal management, Energy Convers. Manag. 101 (2015) 278–284.
[22] J. Lamb, C.J. Orendorff, L.A.M. Steele, S.W. Spangler, Failure propagation in multi-cell lithium ion batteries, J. Power Sources 283 (2015) 517–523.
[23] M. Nofal, Y. Pan, S. Al-Hallaj, Selective laser sintering of phase change materials for thermal energy storage applications, Procedia Manuf. 10 (2017) 851–865.
[24] M. Nofal, S. Al-Hallaj, Y. Pan, Experimental investigation of phase change materials fabricated using selective laser sintering additive manufacturing, J. Manuf. Process. 44 (Aug. 2019) 91–101.
[25] A. Mills, S. Al-Hallaj, Simulation of passive thermal management system for lithium-ion battery packs, J. Power Sources 141 (2) (2005) 307–315.
[26] Superior Graphite Co., Industry Week, 2001. [Online]. Available: https://superiorgraphite.com/.
[27] S. Himran, A. Suwono, G.A. Mansoori, Characterization of alkanes and paraffin waxes for application as phase change energy storage medium, Energy Sources 16 (1) (1994) 117–128.
[28] M. Doyle, T. Fuller, J. Newman, Modeling of galvanostatic charge and discharge of the lithium/ polymer/insertion cell, J. Electrochem. Soc. 140 (6) (1993) 1526–1533.
[29] T.F. Fuller, M. Doyle, J. Newman, Simulation and optimization of the dual lithium ion insertion cell, J. Electrochem. Soc. 141 (1) (1994) 1–10.
[30] L. Song, J.W. Evans, Electrochemical-thermal model of lithium polymer batteries, J. Electrochem. Soc. 147 (6) (2000) 2086–2095.
[31] C. Zhang, K. Li, S. McLoone, Z. Yang, "Battery modelling methods for electric vehicles – a review, 2014 European Control Conference, ECC 2014, 2014, pp. 2673–2678.
[32] L. Gao, S. Liu, R.A. Dougal, Dynamic lithium-ion battery model for system simulation, IEEE Trans. Compon. Packag. Technol. 25 (3) (2002) 495–505.
[33] Y. Hu, S. Yurkovich, Linear parameter varying battery model identification using subspace methods, J. Power Sources 196 (5) (2011) 2913–2923.
[34] R.C. Kroeze, P.T. Krein, Electrical battery model for use in dynamic electric vehicle simulations, PESC Record – IEEE Annual Power Electronics Specialists Conference, 2008, pp. 1336–1342.
[35] M. Salameh, S. Wilke, B. Schweitzer, P. Sveum, S. Al-Hallaj, M. Krishnamurthy, Thermal state of charge estimation in phase change composites for passively cooled lithium-ion battery packs, IEEE Trans. Ind. Appl. 54 (1) (2018) 426–436.
[36] S. Al Hallaj, J.R. Selman, Novel thermal management system for electric vehicle batteries using phase-change material, J. Electrochem. Soc. 147 (9) (2000) 3231–3236.
[37] A. Greco, X. Jiang, D. Cao, An investigation of lithium-ion battery thermal management using paraffin/porous-graphite-matrix composite, J. Power Sources 278 (2015) 50–68.
[38] H. Ghasemi Bahraseman, E.M. Languri, J. East, Fast charging of thermal energy storage systems enabled by phase change materials mixed with expanded graphite, Int. J. Heat Mass Transf. 109 (2017) 1052–1058.
[39] S. Wu, T.X. Li, T. Yan, Y.J. Dai, R.Z. Wang, High performance form-stable expanded graphite/stearic acid composite phase change material for modular thermal energy storage, Int. J. Heat Mass Transf. 102 (2016) 733–744.
[40] X. Yang, Y. Yuan, N. Zhang, X. Cao, C. Liu, Preparation and properties of myristic-palmitic-stearic acid/expanded graphite composites as phase change materials for energy storage, Sol. Energy 99 (2014) 259–266.
[41] A. Karaipekli, A. Biçer, A. Sarı, V.V. Tyagi, Thermal characteristics of expanded perlite/paraffin composite phase change material with enhanced thermal conductivity using carbon nanotubes, Energy Convers. Manag. 134 (2017) 373–381.
[42] N. Zhang, Y. Yuan, X. Wang, X. Cao, X. Yang, S. Hu, Preparation and characterization of lauric-myristic-palmitic acid ternary eutectic mixtures/expanded graphite composite phase change material for thermal energy storage, Chem. Eng. J. 231 (2013) 214–219.
[43] S. Ramakrishnan, J. Sanjayan, X. Wang, M. Alam, J. Wilson, A novel paraffin/expanded perlite composite phase change material for prevention of PCM leakage in cementitious composites, Appl. Energy 157 (2015) 85–94.